Journal of Marine Science and Technology

Volume 30 | Issue 6 Article 4

Numerical Investigation Of The Uncertainty Of Typhoon Wave Parameters Retrieval Using HF Radar

Toan Duy Dao
Institute of Hydrological & Oceanic Sciences, National Central University, Taoyuan, Taiwan, Republic of China,
toandd@huce.edu.vn

Hwa Chien
Institute of Hydrological & Oceanic Sciences, National Central University, Taoyuan, Taiwan, Republic of China

RESEARCH ARTICLE

Numerical Investigation of the Uncertainty of Typhoon Wave Parameters Retrieval Using HF Radar

Toan D. Dao [a,b], Hwa Chien [a,c,*]

[a] Institute of Hydrological & Oceanic Sciences, National Central University, Taoyuan, Taiwan, ROC
[b] Department of Geodesy, Faculty of Bridges and Roads, Hanoi University of Civil Engineering, Hanoi, Viet Nam
[c] Center for Space and Remote Sensing Research, National Central University, Taoyuan, Taiwan, ROC

Abstract

The aim of this study was to identify the sources of uncertainties of typhoon wave field monitoring using HF radar and to quantitatively assess the bias of the wave parameters, such as significant wave height and mean period, retrieved under various conditions. The strategy was to apply a purely numerical simulation of the Doppler-range spectra and then compare the estimation results to the target. For the quantitative investigation, a numerical test-bed was established. The test-bed was used to simulate the Doppler spectra based on Barrick's (1972) theory by using the input of the directional wave spectra. The typhoon wave spectra were hindcasted using a third-generation wave model. Initially, the uncertainty source from Barrick's theory was identified when comparing the deviations of the estimation results obtained from the idealized case of steady and homogenous fields. The accuracy of the wave height and the mean period was found to be significantly influenced by the angle between the radar-looking direction and the wave direction. Furthermore, two conceptual numerical experiments were designed to evaluate the uncertainties owing to the rotation and the translation of the typhoon wind fields, respectively. The first design focussed on the upper-right quadrant around the maximum wind radius of the typhoon using a virtual radar network that moved along with the typhoon. The second one was a more realistic design in that the virtual radar stations were located on the coastline. The scatter index of the wave height estimated from the second design was found to be approximately twice larger than that obtained using the first design. It was 25% larger for the uncertainty of the mean period. This demonstrated that except for the error from theory, the uncertainty of the estimated wave parameters in type 1 was influenced by the change in the wave generated by the wind field, while that of type 2 was affected by the complicated typhoon wavefield, including the mixed wind waves and swells. The results showed that the error of 0.02 of the scatter index in the case of the wave height could be identified even when no system noise was considered. This error was attributed to the simplification of the coupling coefficient and the weighting function in Barrick's theory. The error was direction dependent and non-negligible. For the typhoon cases, the heterogeneity and rapid changes in the spatial distribution of the wavefield under the influence of the rotating wind fields were the challenging factors for the HF radar wave parameter retrieval. The error increased further under such conditions.

Keywords: High-frequency radar, Directional wave spectrum, Typhoon waves, Wave parameters

1. Introduction

Tropical cyclones (TCs) cause devastating losses to life and property and have major socioeconomic effects worldwide. In particular, East and Southeast Asian countries are severely affected because they are the most frequently struck by typhoons. Since 1980, the intensity of typhoons that have hit the North West Pacific region has increased by 12%−15%, and the proportion of category 4 and 5 typhoons has doubled owing to climate change [1]. The extremely high wind speed and severe sea

Received 27 December 2021; revised 24 May 2022; accepted 9 August 2022.
Available online 10 December 2022

* Corresponding author. Institute of Hydrological & Oceanic Sciences, National Central University, Taoyuan, Taiwan, ROC.
E-mail address: hchien@ncu.edu.tw (H. Chien).

https://doi.org/10.51400/2709-6998.2586

states generated by the typhoons are hazardous to coastal zones, ports, and harbors, as well as marine activities [2,3]. The development of coupled atmosphere-wave-ocean models and data assimilation techniques are the approaches for improving the accuracy of typhoon forecasts [4−11]. As ocean surface waves play a major role in affecting the air−sea exchange of heat, moisture, and momentum fluxes [7,12−14], the wave field is the key factor in real-time monitoring under typhoon conditions [15−24].

Real-time monitoring of typhoon waves is still challenging because of the rigors of in-situ instrument deployment. The high-frequency (HF) coastal radar is a promising alternative because of its large spatial coverage, temporally continuous data, and high success rate [24,25]. The HF coastal radar was originally designed for mapping surface currents in coastal oceans. In over four decades, more than 400 HF radar stations have been installed worldwide for myriad applications [26]. Owing to the advances of the inversion algorithms for radar data analysis, it is currently feasible to retrieve the wave directional spectra over large oceanic areas up to 100 km in range on a high-resolution grid in the order of several hundred meters with a high temporal resolution of approximately 10 min.

The HF coastal radar system can be categorized into two types, namely the cross-loop system and the phased-array system, on the basis of the design of the receiving antenna. The Coastal Dynamics Application Radar (CODAR) and Wave Radar (WERA) systems, which are both commercial systems developed by the US National Oceanic and Atmospheric Administration's Wave Propagation Laboratory in the 1980s and the University of Hamburg in the 1990s, respectively, are two examples of the HF coastal radar system [26]. The Taiwanese HF radar network, which consists of 19 CODAR radar stations around the entire Taiwan island and its outlying islands, was established by the Taiwan Ocean Research Institute (TORI) in 2009 for producing surface current maps in the operational mode. In contrast, systems of phased array antennas can provide more information on phase details and are chosen and scheduled to be implemented at specific sites along with the Taoyuan city, New-Taipei city, and the Yi-lan coastline, where high-resolution wave data are required for coastal protection and hazard mitigation purposes.

Numerous theories have been developed to describe the relationship between the characteristics of HF backscattered signals from the sea surface [27−31]. Barrick [27,28] first proposed a theory explaining the sea-echo signals on the Doppler-range (DR) spectrum. On the basis of Barrick's theory, analytical and semi-empirical methods for retrieving the ocean surface wave parameters have been derived. The inversion algorithms for the retrieval of the significant wave height and mean period were based on the relationship between the second-over the first-order components [32−36]. Accordingly, methods for retrieving directional information have been proposed; they use the energy ratio of two first-order peaks of the DR spectra under an assumed wind and shortwave alignment [37−42].

Note that Barrick's theory is based on a perturbation-theory expansion of the nonlinear hydrodynamic and electromagnetic equations for water and waves. The perturbation theory has a finite radius of convergence in the "smallness parameters." One of these is k_0a, where k_0 is the radio wave spatial wavenumber and a is the ocean wave amplitude, which is taken as half of the significant wave height [43]. When this smallness parameter is unity or greater than one, the entire theory becomes invalid. This limitation has been pointed out by several authors such as [43−46]. In light of this saturation limit, the maximum significant wave height, Hs, should be related to k_0. In typhoon cases, when the wave is higher than the saturation limit, the estimation result of the wave height will be biased.

Other than the saturation limit, the accuracy and effectiveness of the HF radar for typhoon wave monitoring depend on the radar receiver sensitivity, ambient radio noise level, and the validity of the inversion algorithms. In this study, the aim was to quantitatively evaluate the errors inherited from the inversion algorithms. To fulfill the objective, purely numerical investigations were carried out. The key for assessing the errors was an End-to-End simulation (E2ES) system, which was established in the present study and used as a numerical test-bed. On the basis of the End-to-End simulation system, the existing methods for estimating wave parameters were implemented and the uncertainties of the results in the typhoon and normal sea state cases were compared. Factors affecting or degrading the inversion results were addressed.

The remainder of this paper is organized as follows: Section 2 introduces the fundamental theory and methodology. Section 3 discusses the numerical test-bed information. Section 4 presents the assessment of wave estimators under the simple homogeneous wave condition. Sections 5 and 6 describe the setup of the numerical test-bed under the typhoon wave condition and discuss the radar-deduced typhoon wave parameter's uncertainty. Section 7 presents the conclusion.

2. Wave parameter inversion from HF radar sea echo

2.1. Barrick's theory

The Doppler-range spectrum is the level one product of an HF radar system. The DR spectrum represents the distribution of the radar echo intensity as a function of the range and the Doppler frequency shift. It is a result of the backscattered intensity due to the interaction of the electromagnetic (EM) waves in the HF band and ocean surface waves. Typically, the DR spectra exhibit two dominant first-order peaks and two minor second-order peaks at the positive and negative Doppler frequencies. The first-order peaks are induced by the direct backscattering of the transmitted EM waves with the presence of ocean waves traveling in opposite directions [27]. The ocean wave component that induces backscattering features a wavelength one-half of that of the EM wave and is called the Bragg wave. The magnitude of the first-order peak is related to the amplitude, direction, and spreading factors of the Bragg waves. The Doppler frequency shifts of the first-order peaks correspond to the combined effects of the surface current velocity and the celerity of the waves propagating in the approaching or receding directions with respect to the radar site along the radar-looking direction. The second-order peaks consist of broader spectral components, including the double-bounce from the two first-order ocean waves as well as the single bounce from the second-order ocean waves [47]. The double-bounce means that the radio wave has been twice Bragg-scattered with any possible pairs of ocean surface wave spectral components in certain wavenumber vectors before it is received. The application of the boundary perturbation theory [48] can hep to represent the magnitudes of the first-order peaks and second-order components as Eqs. (1) and (2), respectively [27,28]:

$$\sigma^{(1)}(\omega) = 2^6 \pi k_0^4 \sum_{m_2=\pm 1} S(-2m_2 k_0)\delta(\omega - m_2\omega_B) \tag{1}$$

$$\sigma^{(2)}(\omega) = 2^6 \pi k_0^4 \sum_{m_1,m_2=\pm 1} \int_{-\infty}^{\infty}\int_{-\infty}^{\infty} S(m_1 k_1) S(m_2 k_2) \times |\Gamma_T|^2 \delta\left(\omega - m_1\sqrt{gk_1} - m_2\sqrt{gk_2}\right) dpdq \tag{2}$$

In Eq. (1), $m_2 = \pm 1$ denotes the sign of the Doppler shift frequency, ω, that corresponds to the receding and advancing Bragg waves, k_0 is the EM wavenumber vector having the magnitude of k_0, S (.) represents the directional wave spectrum as a function of the wavenumber vector, $\omega_B = \sqrt{2gk_0}$ is the Bragg Doppler frequency, and the delta function constraint is denoted by $\delta(.)$. In (2), k_1 and k_2 are the two ocean wave wavenumber vector components with magnitudes k_1, k_2 and directions θ_{k_1}, θ_{k_2}, respectively, on the coordinate p−q plane, as described in [45]. The double integration in (2) is used to superimpose the effects of the double-bounce of the EM wave with any possible pairs of ocean waves that satisfy the condition of $k_1 + k_2 = -2k_0$. Because of the nonlinear quadruplet wave−wave interactions, the ocean wave wavenumber $k_1 + k_2$ is coupled. Thus, Γ_T is introduced as the total coupling coefficient that represents the contribution of ocean wave−wave interactions between (k_1, k_2) and the effect of the EM wave reflection from the seawater surface. This can be expressed as the summation of the hydrodynamic and electromagnetic second-order coupling coefficients, which are denoted as Γ_H and, respectively [32,45].

$$\Gamma_H = \frac{-i}{2}\left[k_1 + k_2 + \frac{(k_1 k_2 - k_1.k_2)(\omega^2 + \omega_B^2)}{m_1 m_2 \sqrt{k_1.k_2}(\omega^2 - \omega_B^2)}\right] \tag{3}$$

$$\Gamma_{EM} = \frac{1}{2}\left[\frac{\frac{(k_1.k_0)(k_2.k_0)}{k_0^2} - 2k_1.k_2}{\sqrt{k_1.k_2} + k_0\Delta}\right] \tag{4}$$

Herein, $\Delta = 0.011 - 0.012i$ is the normalized seawater impedance value proposed in [45]. In the present study, an end-to-end simulation was established using (1) to (4) to generate the DR spectra with the given ocean wave directional spectrum.

2.2. Wave parameter retrieval methods

Methods for estimating the wave height and period from the HF radar DR spectra can be analytical or semi-empirical. The solution of Eqs. (1) and (2) reveals that the root mean square wave height, H_{rms}, which is the integration of the power density of the wave spectrum, can be derived as a function of the ratio between the total second-over first-order power density of the DR spectra.

$$H_{rms} = \frac{1}{k_0}\left(\frac{2\int_{-\infty}^{\infty}\sigma^{(2)}(\omega)\Big/ w(\eta)d\omega}{\int_{-\infty}^{\infty}\sigma^{(1)}(\omega)d\omega}\right)^{1/2} \tag{5}$$

where $w(\eta)$ is called the weighting function that can be determined by taking the average of the integrations of the normalized total coupling

coefficient and $\eta = \omega/\omega_B$ is the normalized Doppler frequency obtained by dividing by the Bragg frequency. According to Barrick [32], the total first-order power can be defined as the integral of the first-order energy in the Doppler spectral, and the total second-order energy is the integral of the weighted second-order energies over valuable Doppler frequencies. Subsequently, on the basis of the probability nature of the wave height, the significant wave height can be determined.

Furthermore, the empirical formula between H_{rms} and the unweighted ratio of the second-over the first-order powers was proposed by Maresca & Georges [33] and Heron & Dexter [49]. A comparative study conducted by Heron & Heron [50] demonstrated that Barrick's analytical formula for retrieving the root-mean-square wave height performed marginally better than the formulae of Maresca & Georges and Heron et al. In addition, the author proposed an empirical formula as follows:

$$H_{rms} = \frac{\xi}{k_0}\left(\frac{2\int_S (\sigma(\omega) - N)/w(\eta)d\omega}{\int_F (\sigma(\omega) - N)d\omega}\right)^{1/2} \quad (6)$$

Herein, ξ is an additional value called the scaling factor and was 0.551 in the study described in [50], N is the background noise, and the first and second integrals are denoted as F and S, respectively. Furthermore, the authors of [50] mentioned that when the wind direction is within 15° of orthogonality to the radar bearing, the algorithm of the root-mean-square wave height retrieval should not be applied. The accuracy of the analytical method can be influenced by the unrealistic idealized assumption in Barrick's theory, ocean wave spectral characteristics, sampling error, and the signal-to-noise ratio (SNR) of the Doppler spectral components. On the basis of practical experience, Barrick [32] suggested that the accuracy of the significant wave height estimation depends mostly on the value of k_0H_{rms}; according to the perturbation theory, the favorable range is $0.1 \le k_0H_{rms} \le 1$ [32,43,45]. This implies that the frequency HF frequency band should be carefully selected on the basis of the sea state [32,43,45,51].

In order to retrieve the mean wave period from the HF radar Doppler spectra, the weighted second-order Doppler spectrum was treated as the wave frequency spectrum; an analytical formula for the wave period estimation is given as follows [32]:

$$T_m = \frac{2\pi}{\omega_B}\left(\frac{\int_{0,1}^{1,\infty} \sigma^{(2)}(\omega) \Big/ w(\eta)d\eta}{\int_{0,1}^{1,\infty} |\eta - 1|\sigma^{(2)}(\omega) \Big/ w(\eta)d\eta}\right) \quad (7)$$

where the spectral sidebands on the positive frequency part are assumed to be more significant than the others. The limit range of the integral range in Eq. (6) could be either 0 to 1 or 1 to infinity. This implies that the limit range of the Doppler frequency for the integral in Eq. (7) could be either from 0 to ω_B or from ω_B to a higher value, which should not be larger than twice the Bragg frequency. With the use of the same assumption for retrieving the significant wave height, the bias of the mean wave period is influenced by the factors that affect the uncertainty of the wave height. In Barrick's study [32], the error for the mean period was approximately 12% for $k_0H_{rms} \ge 0.3$ [32]. However, the uncertainty of the method induced by the ocean wave spectral and directional characteristics has not been discussed. In this study, Eqs. (6) and (7) were implemented on a numerical test-bed to assess the performance of the estimators for retrieving the typhoon wave parameters from the HF radar Doppler spectrum.

3. Establishment of numerical test-bed

In the present study, an end-to-end simulation was established using Barrick's theory to assess the errors from the estimation methods under normal and typhoon conditions. This simulation toolbox was designed as a numerical test-bed that simulated the DR spectrum by using the given directional wave spectra, HF radar location and orientation, and the given system noise level as the inputs. The wave parameter estimators were then applied to the simulated DR spectra, and the results were compared with the known targets for assessing the accuracy under various wave spectral and directional characteristics.

3.1. Modules in E2ES

To simulate the HF radar sea-echo DR spectrum, we followed [45] to rewrite Eq. (2) as a function of the non-dimensional Doppler frequency. The directional wave spectra used as inputs for the simulation of the DR spectra were generated using two approaches. For simple homogeneous wave fields, the JONSWAP spectrum [52], Longuet–Higgins' directional spreading model [53],

and Mitsuyasu's parameterization of the spreading factor [54] were adopted to generate the directional spectra concerning various wind speeds, wind directions, and spreading factors. For more realistic and complicated sea states, such as those during the passage of monsoon fronts and typhoons, the directional spectra were obtained from the third-generation (3G) wave model over the spatial domain driven by high-resolution surface wind fields. The flow of the simulation was as follows (Fig. 1):

(1) Determine the magnitudes of the spectral components of the two coupling waves in the double-bounce scene. The magnitude is retrieved from the input directional wave spectrum at the coupled wavenumber vectors calculated by solving the nonlinear equations [45].
(2) Normalize the coupling coefficients that correspond to the abovementioned wavenumber vectors by using Eqs. (3) and (4).
(3) Substitute the results of the previous two steps into the normalized equation, and then, estimate the second-order components in the DR spectrum by taking integrating over the wavenumber domain.
(4) Repeat steps (1)–(3) for each normalized Doppler frequency to obtain the entire DR spectrum.
(5) Add background noise on the Doppler frequency and range domain.

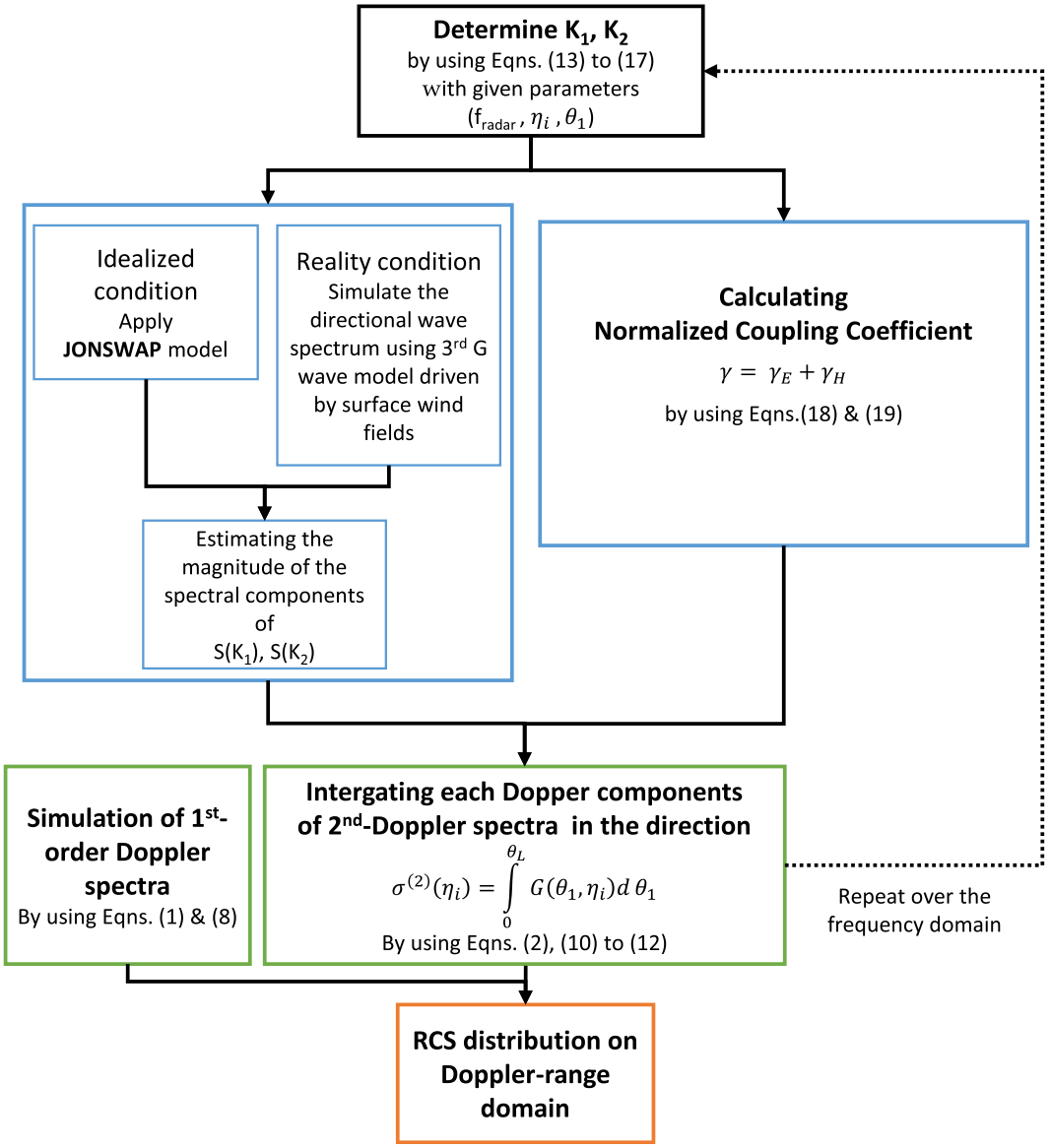

Fig. 1. Flowchart of HF radar Doppler spectra simulation.

3.2. Validation of E2ES

In order to validate the E2ES toolbox, idealized examples with various combinations of wind speed at 10 m in height (U10) from the sea surface, the non-dimensional fetch, $\tilde{\chi}$, and wind directions were given, and the simulation results were characterized with respect to the inputs. The minimum spreading factor "s" in Longuet–Higgins' formula was set to 1 for the shortest wave component of 1 m in wavelength. Figure 2 illustrates an example of noise-free cases from the E2ES toolbox, depicting the effects of changing the wave direction, wind speed, and radar operating frequency to a DR spectral shape. First, Fig. 2(a) illustrates the shifting of the spectral shape from asymmetric to symmetric, corresponding to the increase in θ_w, which is the angle between the wave direction and the radar beam azimuthal orientation. When the alignment of the wave propagating direction and the radar-looking direction was formed, one side of the spectral power reduced. The symmetry of the two first-order peaks as well as that of the second-order peaks was also influenced by the wave directionality.

Figure 2(b) illustrates the effect of the wind speed on the energy of the second-order component. The power of the radar signals significantly increased at the second-order components with increasing wind speed. The dominant peaks of the second-order components also moved towards the first-order peaks as the wavelength grew longer with the increasing wind speed. The characteristics of the first-order and second-order results shown in Fig. 2(a) and (b) agreed with the findings of the previous study [45]. As the wave direction and its directional spreading width strongly influenced the ratio between the spectral powers of the two second-order sidebands surrounding a stronger Bragg peak. The rotating and inhomogeneous wind fields of typhoons and the corresponding complexity of wave directionality played crucial roles in the inversion of wave parameters.

Figure 2(c) shows the magnitudes and the shape of the Doppler spectral corresponding to the frequency band of the HF radar system. The second-order peaks shifted away from the first-order peaks and reduced in the magnitude corresponding to the decrease in the HF radar frequency. This separation made the identification of the first- and second-order peaks easier on the Doppler spectra for lower-band HF radar with the absence of noise. However, there was no doubt that the background noise would be present in reality, and this made the selection of the radar frequency band a trade-off process. Very high frequency band results blurred the gap between the first- and second-order peaks; meanwhile, the second-order peaks were too weak and vanished in the noise for the lower-frequency radar system. Screening of the background radio frequency and preliminarily understanding the ocean wave characteristics in the target area were thus essential prior to the determination of the radar frequency and radar station installation.

Note that one can identify the singularity points at the frequencies $\pm 2^{1/2}\omega_B$ and $\pm 2^{3/4}\omega_B$ in Fig. (2); they were caused by the characteristics of the hydrodynamic and electromagnetic coupling coefficients. In short, the phenomena mentioned above were consistent and agreed well with the known behavior of the DR spectra. The current E2ES testbed could thus be used in the next section for evaluating the errors from the estimation methods.

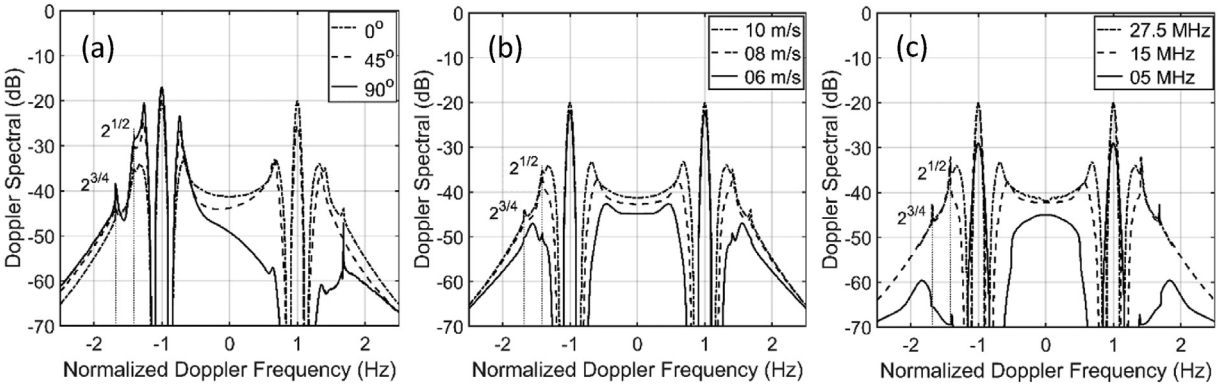

Fig. 2. Examples of simulated Doppler spectra generated using the JONSWAP spectrum form and Longuet–Higgins' directional spreading function with varying initial parameters. Panel (a) shows the simulated Doppler spectra using the following initial parameters: f_{Radar} = 27.5 MHz, U_{10} = 10 m/s, $\theta_N = 0°$, and $\alpha_w = 0°$, 45°, and 90°; panel (b) shows the simulated Doppler spectra using the following initial parameters: $f_{Radar} = 27.5$ MHz, $\theta_N = 0°$, $\alpha_w = 90°$, and $U_{10} = 6$, 8, 10 m/s; panel (c) shows the simulated Doppler spectra with the following initial parameters: $U_{10} = 10$ m/s, $\theta_N = 0°$, $\alpha_w = 90°$, and $f_{Radar} = 27.5$, 15, and 5 MHz.

4. Uncertainty of wave parameter estimation for steady homogeneous wave field

For steady homogeneous wave fields, the JONSWAP spectrum, Longuet–Higgins wave directional spreading model, and Mitsuyasu directional spreading factor parameterization were used to generate the directional wave spectrum. In this numerical test-bed, the operating radar frequency was 27.5 MHz; the wind speed ranged from 5 to 15 m/s. The frequency range of $|0.4|\omega_B - |1.6|\omega_B$ was used to calculate the integral of the second-order Doppler spectra in Eqs. (6) and (7). The scaling factor, ξ, was set to 0.551 [50]. The nulls denoting the boundary between the first- and second-order Doppler spectra were identified by searching for the minimum spectrum over the Doppler frequency area range from the first-order peaks limited by the maximum radial velocity.

This study firstly focused on the dependency of the errors on wave directionality. Figure 3(a) and 3(b) show the comparisons of the estimated results to the given targets at a noise level of −25 dB signal-to-noise ratio. The details of the wave parameter comparisons are presented in Tables 1 and 2. As an initial statistical result, the error indexes of the wave height varied from 0.08 to 0.77 m for RMSE and from 0.022 to 0.141 for SI, while they ranged from 0.26 to 1.02 s and from 0.023 to 0.052 for the RMSE and SI of the mean period, respectively. Two primary reasons were addressed to explain the source of error. Firstly, the second-order components on the Doppler spectrum in Barrick's approach are the results of a double-bounce effect, upon which, the transmitted signal interacts twice with a pair of wave components of two specific wavenumbers before being received. Under such conditions, two mechanisms dominate the return signal characteristics, i.e., the diffractive resonant scattering of electromagnetic waves and the quadruplet wave–wave nonlinear interaction. The coupling coefficient was introduced by Barrick to represent the combined effects of the two abovementioned mechanisms. Secondly, in terms of estimators, an approximation called the weighting function was used to reduce the dimensionality of the coupling coefficient from two dimensions (kx, ky) to a single

Table 1. Uncertainty of radar-deduced wave height radar using numerical E2ES under steady homogenous wave field.

θ_w	Error Indexes of Wave Height Estimation						
	r	RMSE (m)	MAE (m)	SI	Bias (m)	Slope	Intercept
0	0.997	0.53	0.41	0.141	0.41	0.774	−0.05
5	0.997	0.52	0.41	0.138	0.41	0.778	−0.05
10	0.997	0.49	0.39	0.130	0.39	0.788	−0.05
15	0.997	0.45	0.35	0.117	0.35	0.806	−0.04
20	0.997	0.39	0.30	0.102	0.30	0.829	−0.03
25	0.997	0.31	0.24	0.084	0.24	0.857	−0.01
30	0.997	0.23	0.17	0.067	0.17	0.888	0.01
35	0.997	0.14	0.09	0.051	0.08	0.920	0.05
40	0.998	0.08	0.06	0.038	−0.01	0.952	0.09
45	0.998	0.13	0.10	0.029	−0.10	0.982	0.13
50	0.998	0.24	0.21	0.024	−0.21	1.005	0.20
55	0.999	0.35	0.30	0.022	−0.30	1.028	0.25
60	0.999	0.45	0.38	0.024	−0.38	1.047	0.31
65	0.999	0.54	0.46	0.025	−0.46	1.062	0.36
70	1.000	0.62	0.53	0.027	−0.53	1.074	0.41
75	1.000	0.68	0.59	0.029	−0.59	1.082	0.45
80	1.000	0.73	0.63	0.030	−0.63	1.088	0.48
85	1.000	0.76	0.65	0.031	−0.65	1.092	0.50
90	1.000	0.77	0.66	0.031	−0.66	1.093	0.51

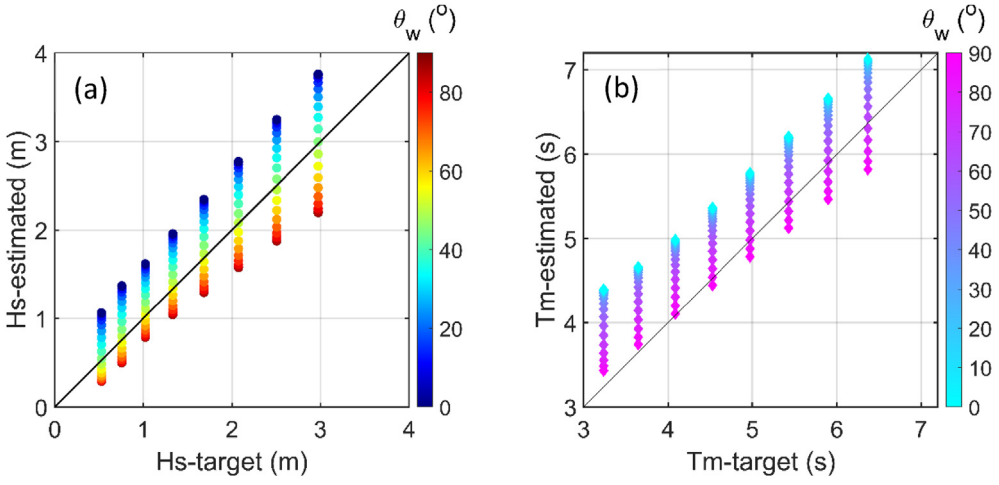

Fig. 3. Effect of varying the wave-to-radar look angle, θ_w, to wave parameters estimated from simulated Doppler spectra. Panels (a) and (b) show the sensitivity test of Hs and Tm, respectively. Here, the wind speed is in the range of 5–15 m/s; the non-dimensional fetch, $\tilde{\chi} = 10^4$; an operating radar frequency of 27.5 MHz was used.

Table 2. Uncertainty of radar-deduced mean wave period radar using numerical E2ES under steady homogenous wave field.

θ_w	Error Indexes of Mean Period Estimation						
	r	RMSE (s)	MAE (s)	SI	Bias (s)	Slope	Intercept
0	1.000	0.33	0.23	0.052	0.16	0.763	1.0
5	1.000	0.28	0.21	0.050	0.07	0.771	1.0
10	0.999	0.26	0.20	0.046	−0.04	0.783	1.1
15	0.999	0.30	0.22	0.043	−0.15	0.795	1.1
20	0.999	0.38	0.27	0.040	−0.26	0.805	1.2
25	1.000	0.48	0.37	0.037	−0.37	0.813	1.3
30	1.000	0.58	0.47	0.035	−0.47	0.819	1.3
35	1.000	0.67	0.55	0.034	−0.55	0.825	1.4
40	0.999	0.75	0.63	0.032	−0.63	0.831	1.4
45	0.999	0.82	0.69	0.031	−0.69	0.839	1.5
50	0.998	0.86	0.73	0.031	−0.73	0.842	1.5
55	0.998	0.91	0.77	0.029	−0.77	0.851	1.5
60	0.998	0.94	0.80	0.028	−0.80	0.859	1.5
65	0.998	0.97	0.82	0.026	−0.82	0.866	1.5
70	0.998	0.99	0.84	0.025	−0.84	0.873	1.5
75	0.998	1.00	0.86	0.024	−0.86	0.878	1.4
80	0.998	1.02	0.87	0.024	−0.87	0.881	1.4
85	0.998	1.02	0.88	0.023	−0.88	0.884	1.4
90	0.998	1.02	0.88	0.023	−0.88	0.884	1.4

dimension (Doppler frequency) by taking the averaged value over the normalized directional distribution. The minor factors included smooth techniques and constant scaling factors.

As inferred from Fig. 3(a), the estimated wave height perfectly fit the targets when the angle between the radar-looking direction and the wave direction, θ_w, was close to 45°, and exhibited overestimation and underestimation corresponding to the decrease or increase in θ_w. The bias of the estimated Hs could reach the maxima of approximately +40% and −25% when θ_w was equal to 0° and 90°, respectively. Figure 3(b) shows a robust linear relationship between the estimated T_m and the target values for different θ_w. The data point did not cover the 1-to-1 diagonal line. The slope was approximately 0.8, which agreed with the discussion in previous studies [32,55]. The comparison results illustrated that the bias estimation of the radar-deduced wave parameters was not uniformly distributed over the spatial domain even under the homogeneous wave field condition. The wave direction was crucial information for the correction of the systematic bias. In addition, narrower wave directional spreading rapidly degrade the performance of the wave estimators, particularly when θ_w is close to 90° [33]. Note that the wave directional spreading width computed from Mistuyasu's parameterization function is proportional to the rise of wave frequencies, which are higher than the peak frequency. In the higher Bragg wavebands, the directional spreading features were broader, thus reducing the bias. This result agreed with the scenario mentioned in [33] and should be considered for assessing the performance of radar-deduced wave parameters.

Second, the radar signal-to-noise ratio strongly affected the accuracy of the estimated wave parameters. The lower radar SNR incurred a higher bias and increased the sensitivity of the results to θ_w. Both of these issues tended to increase the uncertainty of the radar-deduced wave parameters.

Third, the uncertainty of the estimated wave height and mean period could be influenced by different sea states containing different percentages and directions of the swell and wind waves. However, the implementation of the numerical test-bed using a single radar station was limited. A dual-radar system and theoretical methods are needed for assessing the error of the radar-deduced wave height as well as other wave parameters under the mixed-wave field conditions.

Therefore, it could be concluded that the essential factors that affected the HF radar performance under steady and homogeneous conditions were the wave-to-radar angle, radar SNR, and wave directional spreading characteristics. The wave directionality factors, including the angle between the peak wave direction and the radar-looking direction, and the directional spreading width played critical roles in affecting the uncertainty of the estimation results. Maresca & Georges [33] also discussed a case wherein 16 is the threshold of the spreading factor "s" for the Bragg wavebands. An accurate estimation of Hs is impaired when "s" is greater than the threshold (narrower spreading width).

5. Uncertainty of wave parameter estimation for typhoon wave field

5.1. Numerical model of typhoon waves

In order to assess the uncertainties of radar-deduced wave parameters under the passage of typhoons, the non-parameterized directional wave spectra generated from the third-generation wave model were used as the inputs of the test-bed. Hindcast directional spectra from September 23 to 29, 2015, during Typhoon Dujuan (category 4)-caused landfall on the eastern coast of Taiwan (Fig. 4) were chosen as the typhoon cases. The max Hs of 16 m was measured by a wave buoy station at the northeast coast of Taiwan during the typhoon [56] and caused substantial damage to the coastal structures. The trajectory, intensity of Typhoon

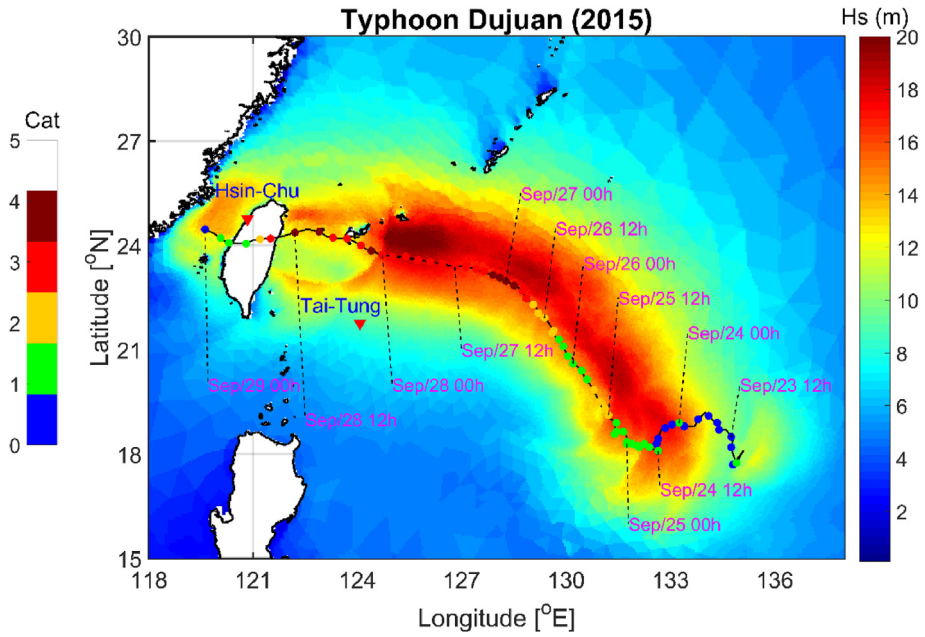

Fig. 4. Map of the maximum significant wave height during Typhoon Dujuan in 2015. The value of the wave height was generated from the third-generation wave model.

Dujuan, and the simulated max Hs over Northwestern Pacific that occurred in this period are illustrated in Fig. 4.

For simulating the unsteadiness and spatial heterogeneity of the typhoon wave characteristics near the maximum wind radius, the directional spectra were hindcasted using the DHI MIKE-21 3-generation spectral wave (SW) model on an unstructured grid domain that covered the entire Northwestern Pacific. The wave model was driven by an ultra-high-resolution (1 km × 1 km) wind field, which was data assimilated and provided by the typhoon research group at Department of Atmospheric Sciences, National Central University, Taiwan. To reconstruct the unsteady and heterogeneous wave field around and the maximum wind radius near the typhoon eye, an unstructured grid was designed to be finer than 3 km in spatial resolution along the typhoon trajectory.

In-situ data for comparisons were recorded by the Hsin-Chu coastal buoy and the Tai-Tung offshore buoy, and their locations are denoted in Fig. 4. Both the Hsin-Chu and the Tai-Tung offshore buoys were developed and deployed by the Coastal Ocean Monitoring Center (COMC) of the National Cheng Kung University (NCKU), Taiwan, in 1997 and 2006, respectively, and are currently managed by the Central Weather Bureau (CWB), Taiwan. The Hsin-Chu buoy was deployed at 24.762770°N, 120.842770°E, with a water depth of 17 m, and the Tai-Tung offshore buoy was deployed at 21.766390°N, 124.074170°E, at a water depth of 5000 m [19]. As for the buoy's structure, the buoy was built in the discus type with a diameter of 2.5 m. Solar panels and onboard batteries were used to provide power for the buoy systems under all possible weather conditions. At least two of the following data transmission devices, which use radio telemetry, Groupe Spécial Mobile (GSM), General Packet Radio Service (GPRS), or Iridium satellite communications, were equipped to transmit the real-time data to the data center. In terms of measurements, the buoys could observe ocean currents, surface waves, and other meteorological observations, such as wind speed, wind direction, air temperature, surface water temperature, and barometric pressure. For the wave measurements, the heave, pitch, and roll accelerometers with a sampling of 2 Hz for 10 min every hour were installed inside the buoys. Then, COMC developed and implemented a data quality checking system, which ensured the quality of the in-situ measurements. Forty-one wave frequencies ranging from 0.05 to 0.4 Hz with a frequency resolution of 0.0085 Hz were used to analyze the directional wave spectra onsite at the buoys. The Fourier series expansion was used to estimate the directional spectrum. Finally, the Hs comparisons of the model output to the observation are shown in Fig. 5(a) and (b).

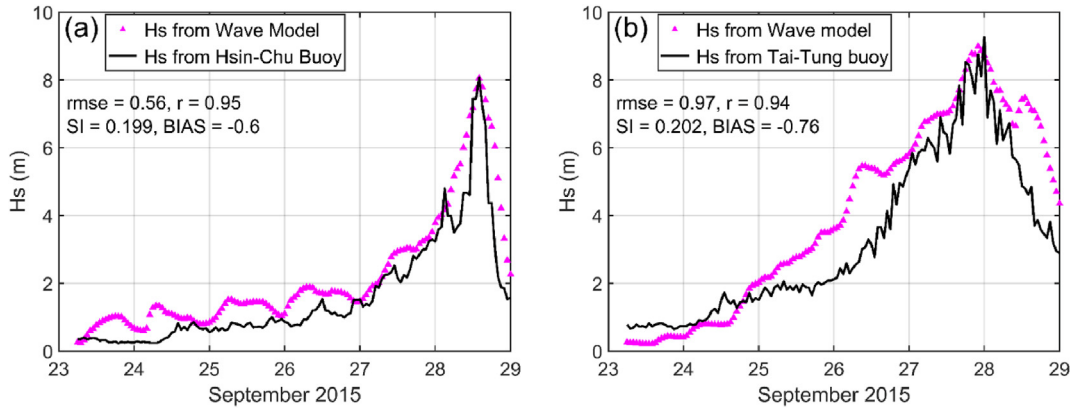

Fig. 5. Comparison between in-situ significant wave height measured from buoys and the modeled value. Panels (a) and (b) present the comparison of time-series significant wave height generated from the wave model and that recorded at Hsin-Chu and Tai-Tung offshore buoys (Fig. 4), respectively.

Examples of the directional wave spectra near the maximum wind radius of approximately 50 km of the eye in various azimuthal positions relative to the eye are shown in Fig. 6. The results showed that the typhoon wave directional spectra exhibited extreme spatial heterogeneity, bimodality, and varying directional spreading. In Fig. 6, the most intensified wave power density is accompanied by narrower directional spreading in the upper-right quadrant relative to the typhoon trajectory and eye. Meanwhile, the directional spectra in the left two quadrants relative to the typhoon trajectory show broader directional spreading. The bimodal wave spectrum caused by the simultaneous presence of the swell and wind waves can be observed in the left-hand quadrants. As the characteristics of waves near the typhoon center were complex, we investigated whether this complexity would impair the wave parameter inversion for the HF radar.

5.2. Simulation of DR spectra inside typhoon

To simulate the HF radar Doppler spectra, the information for setting the radar system was needed. According to the requirement of the perturbation theory and the greatest value of the Dujuan typhoon wave height, basic parameters were set up as follows: The operating radar frequency was 5 MHz, the number of Doppler frequency bin was 1024, and the observation range for the wave measurements was assumed to be 120 km. Two types of virtual radar stations, namely the coastal virtual HF network with the attendant of two radar stations, were set up at fixed locations, and the virtual stations were designed to be mobile and moving along with the typhoon translation as examples. For the first case (case 1), the locations of two virtual HF radar stations, R_1 & R_2, which were 50 km apart, were designed on the northeast coast of Taiwan, as shown in Fig. 7(a). Black dots in Fig. 7(a) denote the locations where the DR spectra were generated.

For the second case (case 2), the virtual radar stations were designed to shift along the typhoon translation to allow for an investigation of the error statistics around the maximum wind radius near the typhoon eye throughout the period. The configuration of the virtual radar stations was as shown in Fig. 7(b), focusing on the upper-right typhoon quadrant. Again, the black dots in Fig. 7(b) denote the locations where the DR spectra were generated.

6. Results and discussion

6.1. Uncertainty of estimated wave parameters from coastal virtual HF radar network under passage of typhoons

Typhoon waves feature complicated patterns in the wave directional spectrum, such as the bimodality and azimuthal asymmetry. It is necessary to assess the error indexes of radar-deduced typhoon wave parameters. First of all, the spatial distribution of estimated wave parameters from the virtual HF radar network on the northeast coast of Taiwan island and the given target are shown in Fig. 8. Here, panels (a) and (b) show the spatial variation of the modeled wave height and the mean period at 1200UTC on September 28, 2015, while panels (c) and (d) illustrate the maps of the estimated wave height and mean period estimations.

Figure 8(a) and (c) show that the estimated Hs values were mostly overestimated compared with the targets, while the spatial distribution of the

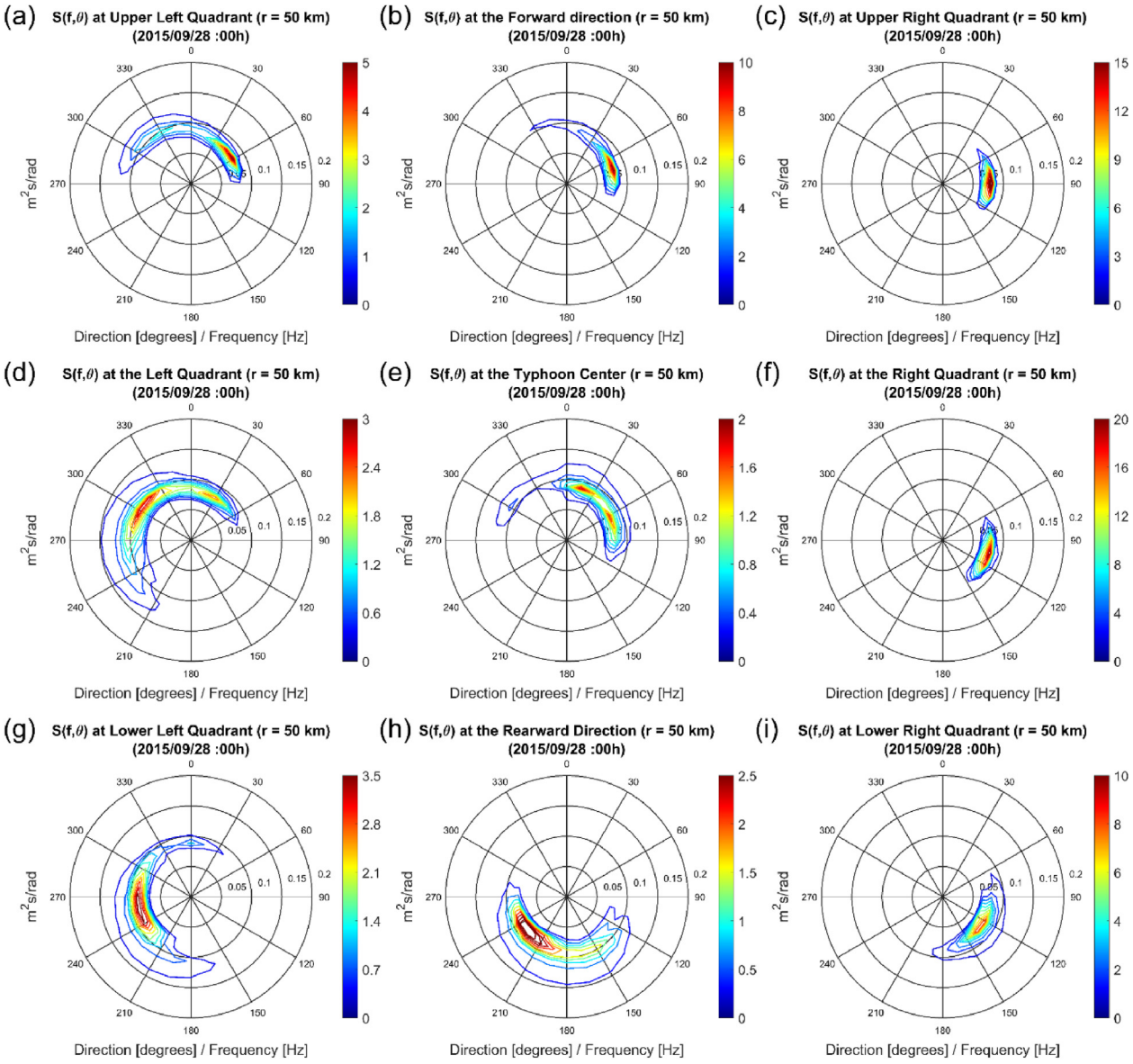

Fig. 6. Directional wave spectra at 00UTC on September 28, 2015, at nine positions. Eight surrounding panels show the directional spectra at locations 50 km from the eye relative to the typhoon translation direction, and the centroid panel presents the directional wave spectrum at the typhoon eye. In detail, (a), (b), and (c) show the directional spectra at the middle of the upper-left, front, and upper-right quadrants, respectively; (d), (e), and (f) represent the directional spectra on the left-hand-side, typhoon center, and right-hand-side quadrants, respectively; (g), (h), and (i) show the directional wave spectra at the lower-left, rear, and upper-left quadrants, respectively.

estimated and the given Hs had the same pattern for both the low and the high sea states. This implied that the overestimation of Hs was only due to the input scaling factor, which could be changed with respect to the radar frequency. In addition, the limited fetch caused small wave-age and provided a broader distribution of the directional spreading during the landfall of Typhoon Dujuan. This might benefit the estimation of the significant wave height. For the mean period comparison, Fig. 8(b) and (d) show that the mean period from the numerical wave model slightly varied over the space domain when Typhoon Dujuan attacked Taiwan's east coast, while the radar-deduced mean period significantly varied on the spatial domain covered by the radar footprint. This variation was mainly due to the change in the radar-to-wave angle as well as the complexity of the typhoon wave directional spreading. To analyze the uncertainty of the estimated wave parameters in case 1, the corresponding error indexes shown in Fig. 9 were calculated during the duration September 27−29, 2015, when Typhoon Dujuan

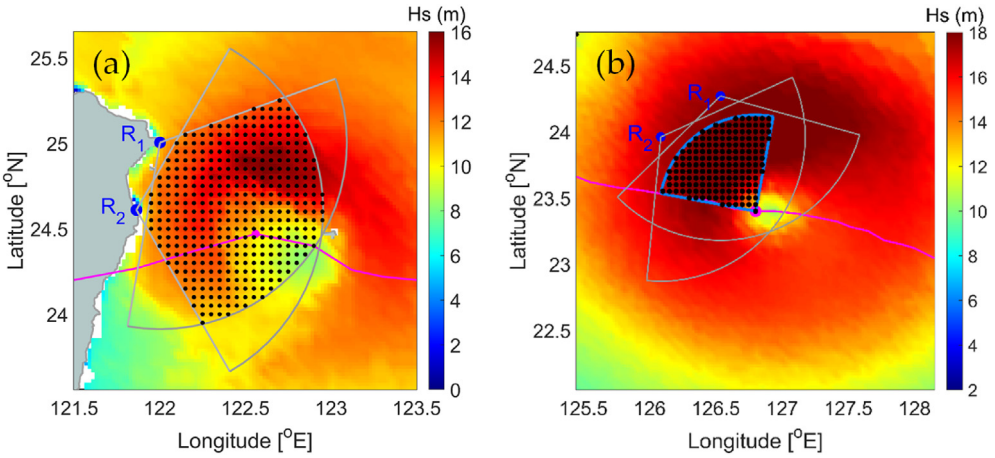

Fig. 7. Configuration of virtual HF radar networks is set up for the test-bed under typhoon conditions. Panel (a) presents a virtual HF radar network with the attendance of two radar sites at the northeast coast of the Taiwan island; panel (b) shows a virtual radar network with two radar sides moving along Typhoon Dujuan's trajectory and focusing on the upper-right quadrant of the typhoon region when it is on the ocean. The grey line shows the coverage area of the virtual HF radar networks; magenta points and lines represent the current location and the trajectory of the typhoon eye, respectively; black dots represent the location of the directional wave spectrum in the domain of the numerical simulation model.

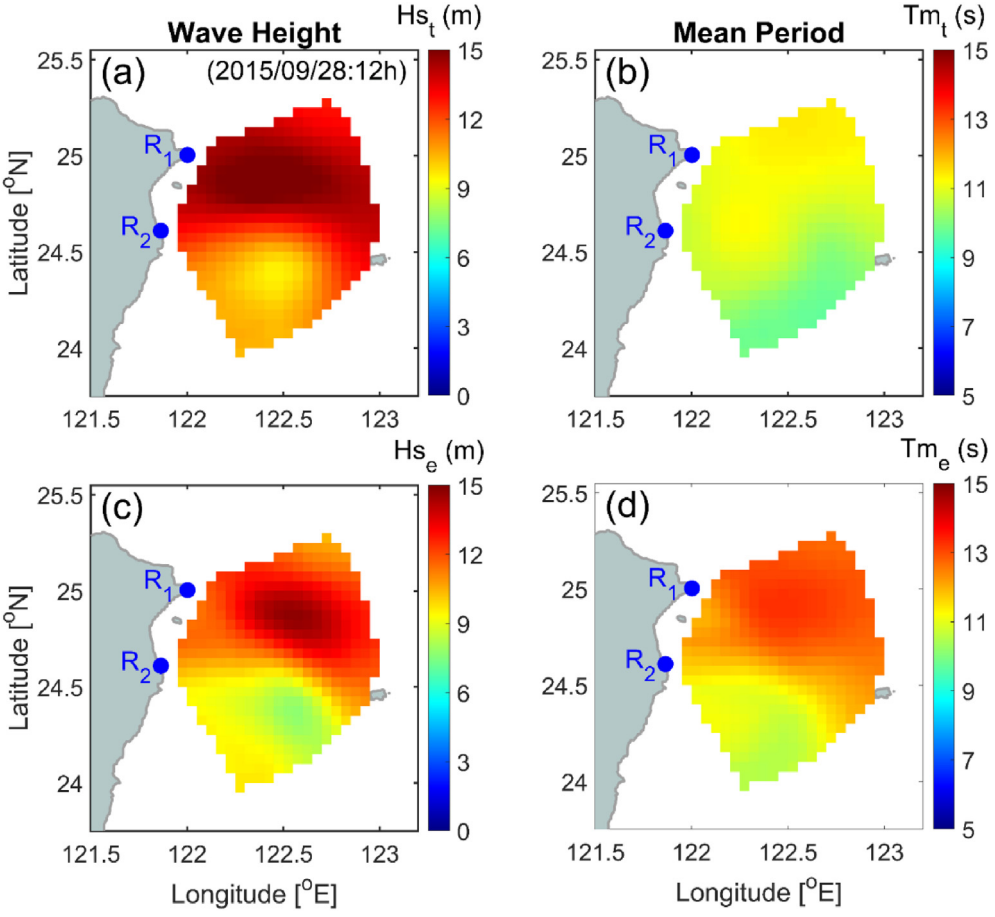

Fig. 8. Spatial distribution of estimated and target wave parameters when Typhoon Dujuan starts to attack the east coast of the Taiwan island. Panels (a) and (b) show the map of the target wave parameters, and (c) and (d) show the spatial distribution of radar-deduced significant wave height and mean period, respectively.

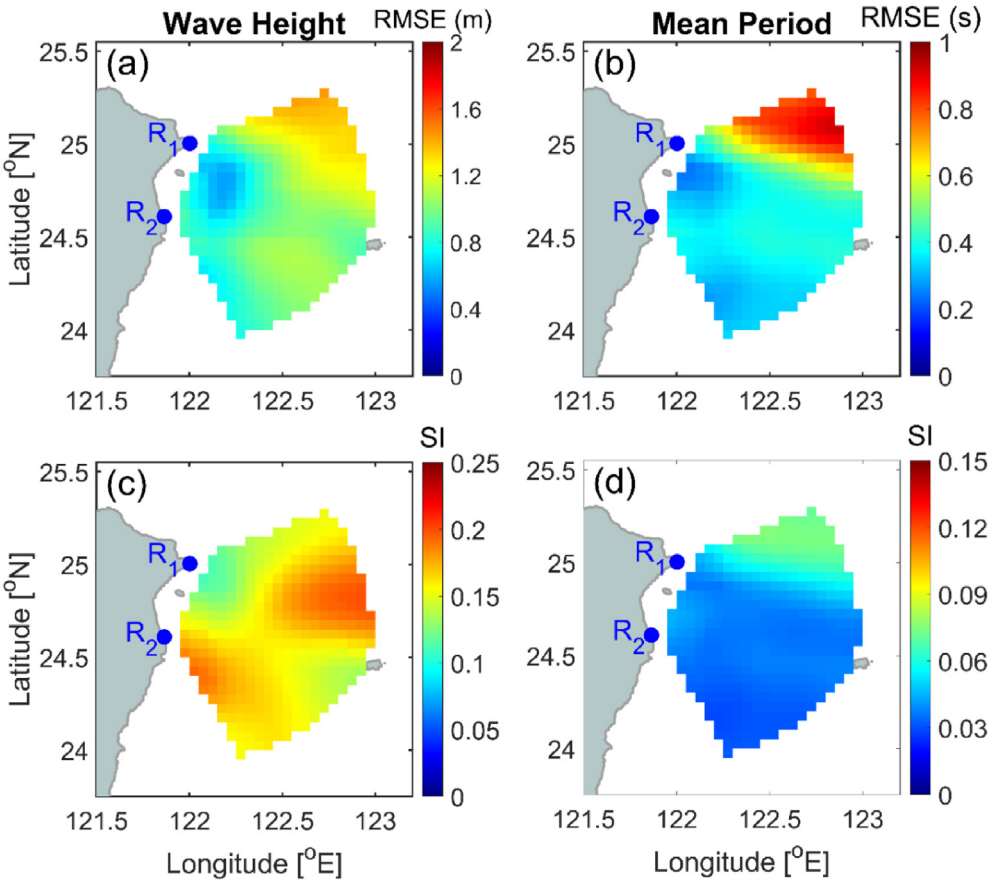

Fig. 9. Spatial distribution of error indexes for typhoon wave height and period. Panels (a) and (b) represent the root-mean-square error of Hs and Tm; panels (c) and (d) represent the scatter index of Hs and Tm, respectively.

started to influence Taiwan's coast. A summary of the statistical values is presented in Table 3.

The spatial distributions of the root-mean-square error (RMSE) and the scatter index (SI) for the significant wave height are shown in Fig. 9(a) and (c), respectively. The value of RMSE and SI for Hs was less than 2.0 m and 0.25, respectively; 1.01 m and 0.16 were the averaged RMSE and SI values, respectively. Fig. 9(a) shows the map of RMSE, which is small in the region located in the middle of two virtual radar stations and increases in others, particularly in the northwest area where larger swells with a narrow directional distribution dominated. The radar-to-wave value was in the range of 30°−60° and might play a role key in this case. The broad directional spreading could also be one of the positive factors for the lower value of the error indexes. The higher value of SI described the large distance between the optimal regression line and the 1-to-1 diagonal line. The estimation result of the wave height shown in Fig. 8(s) indicated that the Hs deduced from the simulated Doppler spectra using Heron's scaling factor was overestimated. This implied that the actual scaling factor between the estimated significant wave height and the target values for the low radar frequency bands and under typhoon conditions should be redetermined. As a result, Fig. 10 illustrates the spatial distribution of the wave height scaling factor under the inhomogeneous condition of wave height, wave direction, and wave directional spreading. The results presented in Fig. 10 show that the wave height scaling factor is inhomogeneous and varies depending on the value of the radar-to-wave angle and the wave characteristics, such as the directional spreading, wave height, and the center frequency of the radar systems.

Table 3. Error indexes of virtual coastal radar-deduced wave height and wave period under the condition of Typhoon Dujuan in 2015.

Statistic Parameters	Hs	Tm
r	0.97 ± 0.02	0.84 ± 0.16
RMSE	1.01 ± 0.24 (m)	0.45 ± 0.19 (s)
Bias	−2.59 ± 0.63 (m)	−1.42 ± 0.4 (s)
SI	0.160 ± 0.022	0.043 ± 0.015
Number of points	18192	

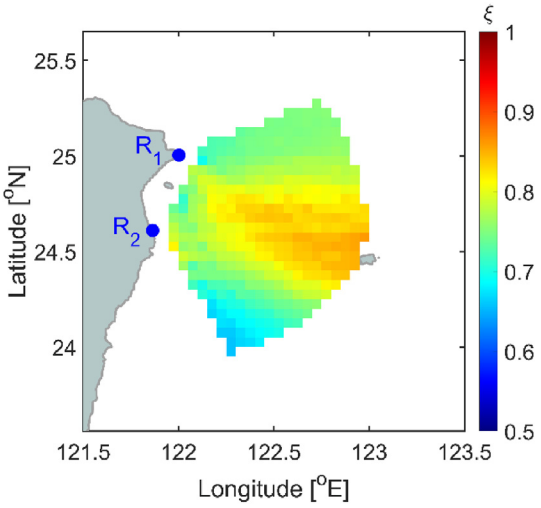

Fig. 10. Spatial distribution of wave height scaling factor within the footprint of the coastal virtual HF radar network.

The uncertainty of the mean period deduced from the simulated Doppler spectrum in case 1 could be assessed using the error indexes (RMSE and SI), which were calculated and are shown in Fig. 9(b) and (d). A summary of the statistical values for the comparison of the mean wave period is presented in Table 3. Figs. 9(b) and (d) show that the RMSE and SI values for the mean period were almost less than 1 s and 0.1, respectively. The average of the two corresponding error indexes was 0.45 s and 0.43. Moroever, the spatial variation of RMSE and SI for the radar-deduced mean period in case 1 had a similar pattern. The higher bias estimation of Tm existed in the northeast area, where the correlation coefficient between the estimated and the target values was low. The combination of larger swells with narrower directional spreading and co-direction between radar bearing and the main wave direction could be factors causing the overestimation of the radar-deduced mean period and producing a higher bias estimation. The averaged error indexes in Table 3 illustrate that the uncertainty of the mean period deduced from the simulated Doppler spectra under typhoon conditions could be acceptable.

6.2. Uncertainty of estimated wave parameters from virtual radar network moving along typhoon translation

In order to assess the uncertainty of the wave parameter estimation near the center of typhoons, a virtual HF radar network with the attendance of two radar stations was set up to move along the typhoon eye trajectory and focus on the upper-right quadrant of the typhoon, as shown in Fig. 7(b). This region consisted of an extreme wind field, considerable wave height, and swells moving in front of the typhoon's direction. Because of the continuously movement of TCs, the monitoring area of the virtual radar network also changed over time. The uncertainty of the estimated result was calculated for each period and over the space domain. The temporal variation of the wave parameter error indexes in the upper-right quadrant of Typhoon Dujuan is shown in Fig. 11, where, the variation of RMSE is represented by red dots, while the value of SI is shown in blue bars.

The results presented in Fig. 11 show that the averaged RMSE and SI of the radar-deduced wave height were 1.3 m and 0.113, respectively, while the values were 0.4 s and 0.052 for the RMSE and SI of the estimated wave period, respectively. The RMSE for Hs varied around 1 m when Typhoon Dujuan moved into the northwest Pacific and rapidly increased to 2 m when the typhoon approached the vicinity of the Taketomi islands, Japan (see Fig. 4). At the same time, the value of SI exceeded 0.2. One possible explanation was that the wave refraction induced by the sheltering effects of small islands generated the directional complicated wavefield, leading to the bias of the end-to-end numerical simulation. However, more efforts and evidences are required to address this issue. A similar phenomenon is found in Fig. 11(b), where the error indexes of the mean period are around 0.45 s for RMSE and less than 0.07 for SI; the two error indexes suddenly increased to more than 0.6 s and 0.1. Nevertheless, the variation of the error indexes for the wave parameter estimation illustrated the excellent performance of the estimators for retrieving the wave height and the mean period under typhoon conditions.

To compare the error indexes of the radar-deduced wave parameters in case 1 and case 2, a comparison of all the data points between the estimated and the target values is shown in Fig. 12. Table 4 lists a summary of the statistical values. In Fig. 12, panels (a) and (b) show the scatter comparison of Hs and Tm in case 1, while panels (c) and (d) show that for case 2. In terms of the wave height comparison, the estimated results in both the cases were almost overestimated as compared to the target values. In Table 4, 1.28 m and 1.46 m were the RMSE of Hs for cases 1 and 2, respectively. It was normal for the RMSE of Hs in case 1 to be smaller than that in case 2 because the average value of the wave height in the open ocean is higher than that in coastal regions, as shown in Fig. 12(a) and (c). Moreover, the scatter index of Hs, which is defined as the RMSE normalized to the target value, was

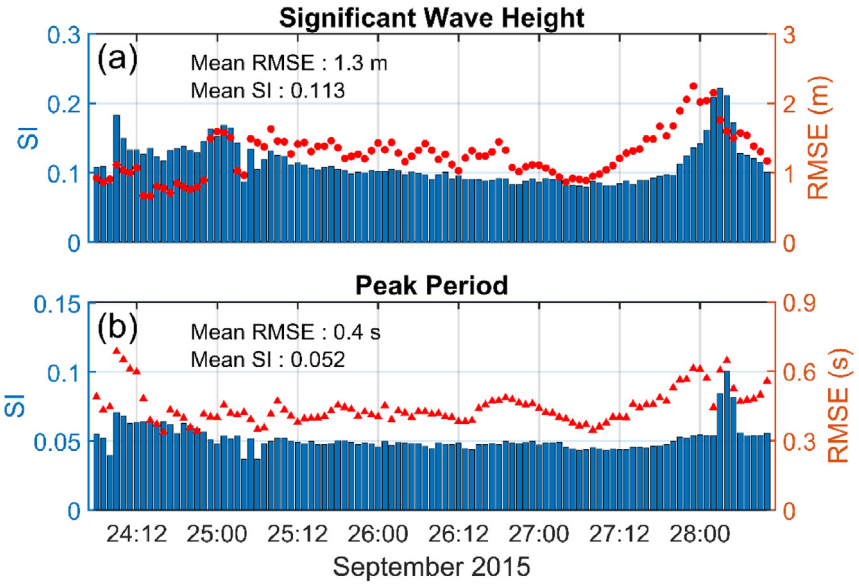

Fig. 11. Temporal variation of error indexes for (a) significant wave height and (b) mean period at the upper-right quadrant of Typhoon Dujuan, which is the case study shown in Fig. 7(b).

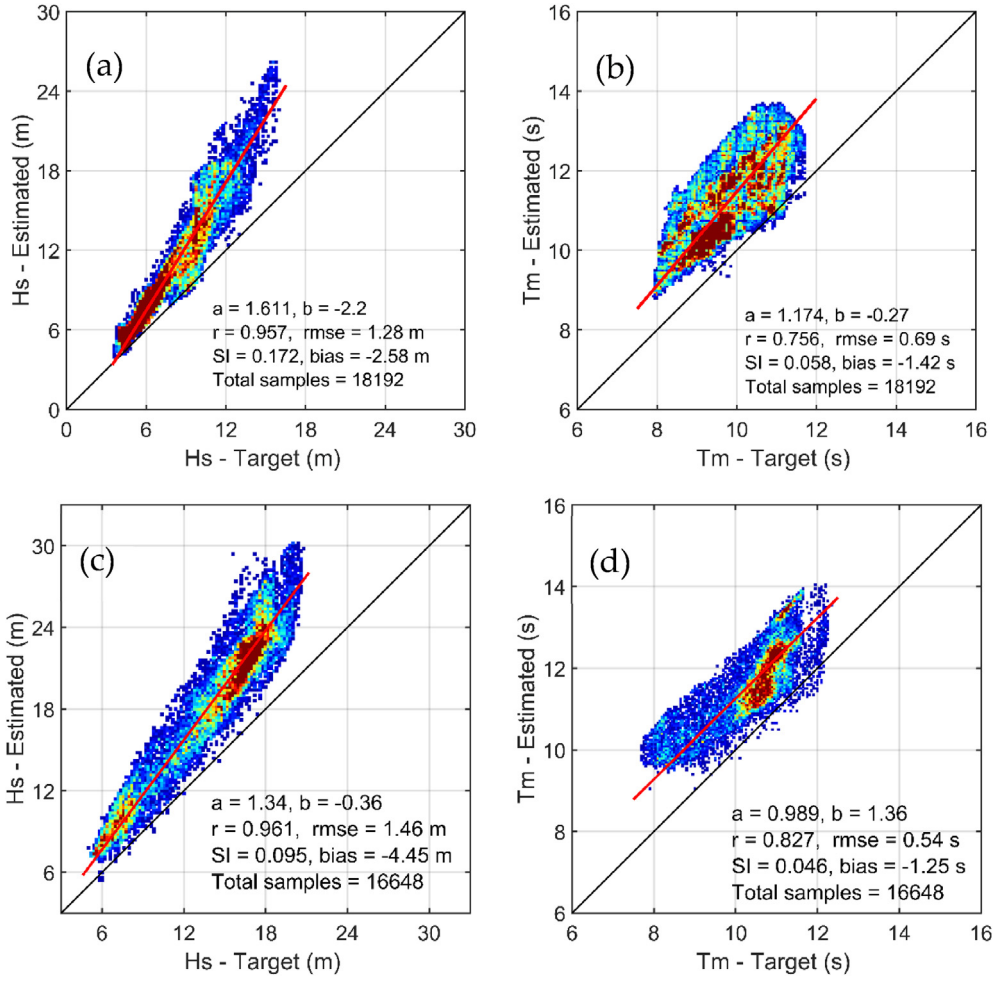

Fig. 12. Scatter comparisons of estimated and target wave parameters under typhoon conditions. Panels (a) and (b) represent the comparison for Hs and Tm using the virtual HF radar system with the attendance of two coastal radar sites, as shown in Fig. 7(a); panels (c) and (d) represent the comparison for Hs and Tm using the virtual HF radar system moving along the typhoon trajectory and focusing on the typhoon upper-right quadrant region, as shown in Fig. 7(b).

17.2% for case 1 and 9.5% for case 2. The scatter index of Hs in case 1 was approximately twice that of case 2. This demonstrated that the bias estimation of Hs in case 1 could be affected by both the method error and the complicated wave field under typhoon conditions, while the uncertainty of the radar-deduced Hs in case 2 was purely influenced by the method error.

For the mean period estimation, the radar-deduced Tm was also overestimated as compared to the target values. One of the reasons was the error of the retrieval algorithm. In addition, the lower frequency for the integral in Eq. (7) might be lower than that of the numerical wave model. In Table 4, 0.69 s and 0.54 s are the RMSE of Tm for cases 1 and 2, respectively, while the SI of Tm is 5.8% for case 1 and 4.6% for case 2. The scatter index of Tm in case 2 was approximately 25% smaller than in case 1. Similarly, the uncertainty of the radar-deduced mean period in case 1 could be influenced by both the method error and the complicated typhoon wave, while the error index of Tm in case 2 was purely affected by the error of the method.

The error indexes of wave parameters in case 2 indicated that the HF radar could perform well for retrieving the typhoon wave parameters in regions around the typhoon center. In this study, even though numerical E2ES cases with more than two virtual radar sites in the HF radar network were not considered and the focus was not on areas near the typhoon center, such as at lower-right or left quadrants, the performance of the HF radar was still excellent. Note that the wave directional spreading width in quadrants that might benefit the HF radar's performance was greater than that in the upper-right quadrant. Therefore, the complexities of the typhoon wave directional spectra included extreme spatial heterogeneity, multiple peaks, and particularly broadened spreading, which might reduce the uncertainty of the estimated parameters. From the perspective of a better radar SNR caused by a greater wave height and broader directional spreading because of rapidly changing wind, these typhoon wave characteristics would make the HF radar suitable for the monitoring task.

Table 4. Statistical parameters of estimated wave parameters in two configurations of HF radar network under extreme typhoon conditions.

Wave Parameters	Statistical Parameters	Case 1	Case 2
Hs	r	0.957	0.961
	RMSE (m)	1.28	1.46
	Bias (m)	−2.58	−4.45
	SI	0.172	0.095
Tm	r	0.756	0.827
	RMSE (s)	0.69	0.54
	Bias (s)	−1.42	−1.25
	SI	0.058	0.046
Number of points		18192	16648
Focusing region		Coastal region	Upper-right quadrant

7. Conclusions

The parameters of ocean surface waves retrieved from the first- and second-order components of the HF radar Doppler spectra might be influenced by numerous factors. Therefore, an assessment of radar-deduced wave parameter's uncertainty under various conditions is necessary. By using the purely numerical tests that included the simulation of the radar Doppler spectra using Barrick's theory and the modeled directional wave spectrum, and the existing wave parameter estimators, this study aimed to investigate the uncertainty of radar-deduced wave parameters under various conditions, such as steady homogeneous and typhoon wavefield conditions, at the free noise level. The numerical experiments were designed from the idealized to a more realistic case to distinguish the error between the theory and the estimators, and to discuss the error sources.

In the case of the homogeneous wave field, the comparison results showed that the angle between the radar-looking direction and the wave direction was one of the crucial factors influencing the uncertainty of the radar-deduced wave parameters. The error indexes of wave height varied from 0.08 to 0.77 m for RMSE and from 0.022 to 0.141 for SI, while they ranged from 0.26 to 1.02 s and from 0.023 to 0.052 for RMSE and SI of the mean period, respectively. The sources of error were discussed. For correcting the estimation results in the case of the steady homogenous wave field, different scaling factors for wave parameters with respect to different radar-to-wave angles would be needed.

Because of the rotating wind fields under typhoon conditions, the uncertainty of radar-deduced wave fields varies continuously and is thus challenging for assessment. Two types of virtual HF radar networks, namely one mobile and moving along with the translation of typhoon and the other fixed on the coastline, were designed to investigate the uncertainty of radar-deduced typhoon wave parameters. In the case of the mobile virtual radar network type, the RMSE and SI of the wave height were 1.46 m and 0.095, and those of the mean period were 0.54 s and 0.046 in the constant typhoon quadrant. Meanwhile, the RMSE and SI of the wave height

were 1.28 m and 0.172, respectively, and those pf the mean period were 0.69 s and 0.058, respectively, in different typhoon quadrants. The errors in the case of type 1 were approximately half of those for the latter type, while they were 25% less for the SI of the mean period. These results indicated that except for the error from theory, the uncertainty of the estimated wave parameters in type 1 was influenced by the change in the wave generated by the wind field, while that in the case of type 2 was affected by the complicated typhoon wavefield, including the mixed wind waves and swells. By comparing the scatter indexes of the estimated wave parameters under the two abovementioned weather conditions, it was found that the SI of the wave height in the case of type 1 under the typhoon wave field was more than four times larger than the SI of the best-fit case for the wave height retrieval under the steady homogenous wave field; it was two times larger for the SI of the mean period. This implied that the heterogeneity and rapid changes in the spatial distribution of the wavefield under the influence of high wind speeds significantly affected the uncertainty of the typhoon wave parameters deduced from the HF radar, particularly measured by coastal systems.

In future works, the shortcomings of Eqs. (1) and (2) can be overcome by using new models for simulating the DR spectra under an arbitrary wave height, which have been developed by Silva et al. [57, 58]. Furthermore, theoretical methods such as the Bayesian method are suggested for implementation in the numerical E2ES to assess the uncertainty of the radar-deduced directional wave spectrum under various weather conditions.

Conflict of interest

The authors declare that there are no conflicts of interest regarding the publication of this paper.

Acknowledgments

The authors would like to express their sincere gratitude to Dr. C.-M Zhang at the DHI Taipei branch office for implementing the typhoon wave model on an unstructured grid. This research was supported by the National Science and Technology council, Taiwan under the project 110-2611-M-008-002.

Appendix

To simulate the radar cross-section (RCS) of HF radar sea echo, Eqs. (1) and (2) were derived in the case of a deep-water region. First, the Doppler frequency and wavenumber were normalized by dividing ω_B and $2k_0$, respectively; Barrick's equation for the first- and second-order components of RCS could then be rewritten as follows [45]:

$$\sigma^{(1)}(\eta) = 4\pi \sum_{m_2=\pm 1} S(-m_2\hat{k}_0)\delta(\eta - m_2) \tag{8}$$

$$\sigma^{(2)}(\eta) = 8\pi \sum_{m_1,m_2=\pm 1} \int_0^{\infty}\int_{-\pi}^{\pi} S(m_1K_1)S(m_2K_2) \times |\gamma|^2 \delta\left(\omega - m_1\sqrt{K_1} - m_2\sqrt{K_2}\right) K_1 dK_1 d\theta_1 \tag{9}$$

where η is the normalized Doppler shift; $\hat{k}_0$ is the unit vector of radio wavenumber; K_1 and K_2 are two normalized wavenumber vectors of two ocean waves, respectively; γ is the normalized coupling coefficient; and θ_1 is the direction of the wavenumber vector K_1. In Eq. (9), the value of m_1, m_2 defines four side-bands of the second-order component of the DR spectra: $m_1 = m_2 = 1$ corresponds to $\eta > 1$; $m_1 = m_2 = -1$ corresponds to $\eta < -1$; $m_1 = 1$ and $m_2 = -1$ correspond to $-1 < \eta < 0$; and $m_1 = -1$ and $m_2 = 1$ correspond to $0 < \eta < 1$.

The two-dimensional nonlinear integral of Eq. (9) could be simplified by transforming Eq. (9) into a single variable because the integrand included the Dirac delta function. Now, the algorithm of second-order components could be expressed as follows:

$$\sigma^{(2)}(\theta_1,\eta) = \int_0^{\theta_L} G(\theta_1,\eta)d\theta_1 \tag{10}$$

$$G(\theta_1,\eta) = 16\pi\left[|\gamma|^2\{S(K_1,\alpha_1)S(K_2,\alpha_2) + S(K_1,-\alpha_1)S(K_2,-\alpha_2)\}\left|\frac{dy}{dh}\right|y^3\right]_{y=\hat{y}} \tag{11}$$

where

$$\left|\frac{dy}{dh}\right| = \left|1 + m_1m_2\frac{y(y^2+\cos\theta_1)}{(y^4+2y^2cos\theta_1+1)^{3/4}}\right|^{-1} \tag{12}$$

with $y = \sqrt{K_1}$. $\hat{y}$ was obtained by solving the following nonlinear equation:

$$\eta - m_1\hat{y} - m_2\left(\hat{y}^4 + 2\hat{y}^2cos\theta_1 + 1\right)^{1/4} = 0 \tag{13}$$

Furthermore, the other parameters were calculated as follows:

$$K_2 = \sqrt{K_1{}^2 + 2K_1cos\theta_1 + 1} \tag{14}$$

$$\theta_2 = sin^{-1}\left(\frac{K_1 sin\theta_1}{K_2}\right) + \pi \tag{15}$$

$$\alpha_1 = \theta_1 \pm (1 - m_1)\pi/2 \tag{16}$$

$$\alpha_2 = \theta_2 \pm (1 - m_2)\pi/2 \tag{17}$$

The value of θ_L denotes the upper limit of integration and can be expressed as $\theta_L = \pi$ when $|\eta| \leq \sqrt{2}$, and $\theta_L = \pi - \cos^{-1}(2/\eta^2)$ when $|\eta| > \sqrt{2}$, respectively. In addition, the normalized coupling coefficient was calculated as follows:

$$\gamma_H = \frac{-i}{2}\left[K_1 + K_2 + \frac{(K_1K_2 - \boldsymbol{K_1}.\boldsymbol{K_2})(\eta^2 + 1)}{m_1 m_2 \sqrt{K_1K_2}(\eta^2 - 1)}\right] \tag{18}$$

$$\gamma_{EM} = \frac{1}{2}\left[\frac{(\boldsymbol{K_1}.\widehat{\boldsymbol{k}}_0)(\boldsymbol{K_2}.\widehat{\boldsymbol{k}}_0) - 2\boldsymbol{K_1}.\boldsymbol{K_2}}{\sqrt{\boldsymbol{K_1}.\boldsymbol{K_2} + \Delta/2}}\right] \tag{19}$$

Thus, based on the expression below, the generation of the RCS of the HF radar sea echo using numerical simulations with the given sea−stage parameters was possible.

References

[1] Mei W, Xie SP. Intensification of landfalling typhoons over the Northwest Pacific since the late 1970s. Nat Geosci 2016;9:753.

[2] Chang CH, Shih HJ, Chen WB, Su WR, Lin LY, Yu YC, et al. Hazard assessment of typhoon-driven storm waves in the nearshore waters of Taiwan. Water 2018;10(7):926.

[3] Roy C, Sarkar SK, Åberg J, Kovordanyi R. The current cyclone early warning system in Bangladesh: providers' and receivers' views. Int J Disaster Risk Reduc 2015;12:285−99.

[4] Liu B, Liu H, Xie L, Guan C, Zhao D. A coupled atmosphere−wave−ocean modeling system: simulation of the intensity of an idealized tropical cyclone. Mon Weather Rev 2010;139(1):132−52.

[5] Chen SS, Curcic M. ocean surface waves in hurricane ike (2008) and superstorm sandy (2012): coupled model predictions and observations. Ocean Model 2016;103:161−76.

[6] Liu Q, Babanin A, Fan Y, Zieger S, Guan C, Moon IJ. Numerical simulations of ocean surface waves under hurricane conditions: assessment of existing model performance. Ocean Model 2017;118:73−93.

[7] Moon JH, Kang KR. Uncertainty and sensitivity of wave-induced sea surface roughness parameterisations for a coupled numerical weather prediction model AU - Kim. Taekyun Tellus A: Dyn Meteorol Oceanogr 2018:1−18.

[8] Wu L, Wang B, Braun SA. Impacts of air-sea interaction on tropical cyclone track and intensity. Mon Weather Rev 2005;133(11):3299−314.

[9] Green BW, Zhang F. Impacts of air−sea flux parameterizations on the intensity and structure of tropical cyclones. Mon Weather Rev 2013;141(7):2308−24.

[10] Soloviev A, Lukas RA, Donelan M, Ginis I. The air-sea interface and surface stress under tropical cyclones, vol. 4; 2013, 12690.

[11] Garg N, Ng EYK, Narasimalu S. The effects of sea spray and atmosphere−wave coupling on air−sea exchange during a tropical cyclone. Atmos Chem Phys 2018;18(8):6001−21.

[12] Fan Y, Ginis I, Hara T. The effect of wind−wave−current interaction on air−sea momentum fluxes and ocean response in tropical cyclones. J Phys Oceanogr 2009;39(4):1019−34.

[13] Chen SS, Zhao W, Donelan MA, Tolman HL. Directional wind−wave coupling in fully coupled atmosphere−wave−ocean models: results from CBLAST-Hurricane. J Atmos Sci 2013;70(10):3198−215.

[14] Veron F, Melville WK, Lenain L. Wave-coherent air−sea heat flux. J Phys Oceanogr 2008;38(4):788−802.

[15] Wright CW, Walsh EJ, Vandemark D, Krabill WB, Garcia AW, Houston SH, et al. Hurricane directional wave spectrum spatial variation in the open ocean. J Phys Oceanogr 2001;31(8):2472−88.

[16] Young IR. Directional spectra of hurricane wind waves. J Geophys Res: Oceans 2006;111(C8).

[17] Hu K, Chen Q. Directional spectra of hurricane-generated waves in the Gulf of Mexico. Geophys Res Lett 2011;38(19).

[18] Montoya RD, Osorio Arias A, Ortiz Royero JC, Ocampo-Torres FJ. A wave parameters and directional spectrum analysis for extreme winds. Ocean Eng 2013;67:100−18.

[19] Doong DJ, Tsai CH, Chen YC, Peng JP, Huang CJ. Statistical analysis on the long-term observations of typhoon waves in the Taiwan sea. J Mar Sci Technol 2015;23(6):893−900.

[20] Bennett VCC, Mulligan RP. Evaluation of surface wind fields for prediction of directional ocean wave spectra during Hurricane Sandy. Coast Eng 2017;125:1−15.

[21] Aouf L, Lefèvre JM, Hauser D. Assimilation of directional wave spectra in the wave model WAM: an impact study from synthetic observations in preparation for the SWIMSAT Satellite Mission. J Atmos Ocean Technol 2006;23(3):448−63.

[22] Fan YM, Günther H, Kao CC, Lee BC. Assimilation of decomposed in situ directional wave spectra into a numerical wave model of typhoon waves. Nat Hazards Earth Syst Sci 2014;14(1):73−80.

[23] Trizna DB. Monitoring coastal processes and ocean wave directional spectra using a marine radar. In: Oceans 2006 - Asia pacific; 2006.

[24] Gurgel KW, Antonischki G, Essen HH, Schlick T. Wellen Radar (WERA): a new ground-wave HF radar for ocean remote sensing. Coast Eng 1999;37(3):219−34.

[25] Castillo-Trujillo AC, Partridge D, Powell B, Flament P. Vorticity balance off the south shore of Oahu, Hawaii, derived by high-frequency radio Doppler current observations. J Phys Oceanogr 2019;49(1):211−25.

[26] Rubio A, Mader J, Corgnati L, Mantovani C, Griffa A, Novellino A, et al. HF radar activity in European coastal seas: next steps toward a Pan-European HF radar network. Front Mar Sci 2017;4(8):1−20.

[27] Barrick DE. First-order theory and analysis of MF/HF/VHF scatter from the sea. IEEE Trans Antenn Propag 1972;20(1):2−10.

[28] Barrick DE. Remote sensing of sea state by radar. In: Ocean 72 - IEEE international conference on engineering in the ocean environment; 1972.

[29] Gill EW, Walsh J. High-frequency bistatic cross sections of the ocean surface. Radio Sci 2001;36(6):1459−75.

[30] Voronovich AG, Zavorotny VU. Measurement of ocean wave directional spectra using airborne HF/VHF synthetic aperture radar: a theoretical evaluation. IEEE Trans Geosci Rem Sens 2017;55(6):3169−76.

[31] Hasselmann K. Determination of ocean wave spectra from Doppler radio return from the sea surface. Nat Phys Sci (Lond) 1971;229:16.

[32] Barrick DE. Extraction of wave parameters from measured HF radar sea-echo Doppler spectra. Radio Sci 1977;12(3):415−24.

[33] Maresca JW, Georges TM. Measuring RMS wave height and the scalar ocean wave spectrum with HF skywave radar, vol. 85; 1980. p. 2759−72.

[34] Wyatt LR, Venn J, Burrows G, Ponsford A, Moorhead M, Heteren JV. HF radar measurements of ocean wave parameters during NURWEC. IEEE J Ocean Eng 1986;11(2):219−34.

[35] Graber HC, Heron ML. Wave height measurements from HF radar. Oceanography 1997;10(2):90−2.

[36] Chen Z, Chen ZZ, Jiang Y, Fan L, Zend G. Exploration and validation of wave-height measurement using

multifrequency HF radar. J Atmos Ocean Technol 2013;30(9): 2189−202.
[37] Long A, Trizna D. Mapping of North Atlantic winds by HF radar sea backscatter interpretation. IEEE Trans Antenn Propag 1973;21(5):680−5.
[38] Fernandez DM, Graber HC, Paduan JD, Barrick DE. Mapping wind directions with HF radar. Oceanography 1997; 10(2):93−5.
[39] Wyatt LR. Shortwave direction and spreading measured with HF radar. J Atmos Ocean Technol 2011;29(2):286−99.
[40] Heron ML, Prytz A. Wave height and wind direction from the HF coastal ocean surface radar. Can J Rem Sens 2002; 28(3):385−93.
[41] Huang W, Gill E, Wu S, Wen B, Yang Z, Hou J. Measuring surface wind direction by monostatic HF ground-wave radar at the eastern China sea, vol. 29; 2004. p. 1032−7.
[42] Li C, Wu X, Yue X, Zhang L, Liu J, Li M, et al. Extraction of wind direction spreading factor from broad-beam high-frequency surface wave radar data. IEEE Trans Geosci Rem Sens 2017;55(9):5123−33.
[43] Wyatt LR. High order nonlinearities in HF radar backscatter from the ocean surface. IEE Proc - Radar, Sonar Navig 1995; 142(6):293−300.
[44] Wyatt L, Green JJ, Middleditch A. HF radar data quality requirements for wave measurement. Coast Eng 2011;58(4): 327−36.
[45] Lipa BJ, Barrick DE. Extraction of sea state from HF radar sea echo: mathematical theory and modeling. Radio Sci 1986; 21(1):81−100.
[46] Lipa B, Nyden B. Directional wave information from the SeaSonde. IEEE J Ocean Eng 2005;30(1):221−31.
[47] Walsh J, Huang W, Gill E. The second-order high frequency radar ocean surface cross section for an antenna on a floating platform. IEEE Trans Antenn Propag 2012;60(10):4804−13.
[48] Rice SO. Reflection of electromagnetic waves from slightly rough surfaces. Commun Pure Appl Math 1951;4(2−3):351−78.
[49] Heron ML, Dexter PE, McGann BT. Parameters of the air-sea interface by high-frequency ground-wave Doppler radar. Mar Freshw Res 1985;36(5):655−70.
[50] Heron SF, Heron ML. A comparison of algorithms for extracting significant wave height from HF radar ocean backscatter spectra. J Atmos Ocean Technol 1998;15(5): 1157−63.
[51] Wyatt L, Green J, Middleditch A. HF radar data quality requirements for wave measurement. Coast Eng 2011;58:327−36.
[52] Hasselmann KP, Barnett T, Bouws E, Carlson HE, Cartwright D, Enke KA, et al. Measurements of wind-wave growth and swell decay during the joint North sea wave project (JONSWAP)8; 1973. p. 1−95.
[53] Michael L-H, Cartwright DE, Smith ND. Observations of the directional spectrum of sea waves using the motions of a floating buoy. In: ocean wave spectra, proceedings of a conference. Easton, Maryland: Prentice-Hall; 1963.
[54] Mitsuyasu H, Tasai F, Suhara T, Mizuno S, Ohkusu M, Honda T, et al. Observations of the directional spectrum of ocean waves using a cloverleaf buoy. J Phys Oceanogr 1975;5(4):750−60.
[55] Lopez G, Conley D, Greaves D. Calibration, validation and analysis of an empirical algorithm for the retrieval of wave spectra from HF radar sea-echo. J Atmos Ocean Technol 2015;33:151216150545004.
[56] Chen WB, Lin LY, Jang JH, Chang CH. Simulation of typhoon-induced storm tides and wind waves for the northeastern coast of Taiwan using a tide−surge−wave coupled model. Water 2017;9(7).
[57] Silva MT, Huang W, Gill EW. High-frequency radar cross section of the ocean surface with arbitrary roughness scales: a generalized functions approach. IEEE Trans Antenn Propag 2021;69(3):1643−57.
[58] Silva MT, Huang W, Gill EW. High-frequency radar cross section of the ocean surface with arbitrary roughness scales: higher order corrections and general form. IEEE Trans Antenn Propag 2021;69(10):6723−38.